DIRECTIONAL BALANCE: A GENERAL DESIGN PRINCIPLE FOR BINARY FRINGE PROJECTION

Anonymous authors
Paper under double-blind review

ABSTRACT

High-speed structured-light imaging often relies on binary-defocusing fringe projection, in which binary patterns are optically low-pass filtered into approximately sinusoidal fringes. Under shallow defocus, error diffusion is the preferred way to preserve sinusoidal fidelity, but its kernel is usually selected by hand or by black-box search, so the direction-dependent phase bias is not explicitly controlled. Rather than correcting this bias at the fringe patterns, we analyze the diffusion kernel itself and introduce a normalized balance coefficient that measures the asymmetry between forward and backward error propagation. The dominant directional phase bias vanishes when this coefficient is zero. This condition yields the Guideline-Based Optimization (GBO) kernels for horizontal and vertical fringes with no additional run-time overhead and no change to the downstream reconstruction process. Unlike sequence-level inter-fringe compensation, our approach does not reorganize the phase-shifting sequence. On real measurements, GBO reduces AE by 17.84% and RMSE by 22.45% relative to the second-best baseline.

1 INTRODUCTION

Recovering dense three-dimensional (3D) shapes from two-dimensional (2D) images is a long-standing challenge in artificial intelligence. Recent advances in sensors, learning-based methods, and computational imaging have made high-quality 3D reconstruction increasingly practical (Zhang & Yau, 2006; Zhang et al., 2019; Khan et al., 2018). The resulting point clouds are now used in object detection, object tracking, and 3D shape feature learning, where both speed and accuracy determine whether a reconstruction algorithm is useful in real systems (Yan et al., 2017; Koh et al., 2022; Li & Cheng, 2022).

Among the available reconstruction techniques, fringe projection profilometry (FPP) has become a dominant active-vision approach because it is low cost, robust, and capable of dense, high-spatial-resolution measurement (Su & Zhang, 2010; Geng, 2011; Quan et al., 2007). FPP encodes the projector coordinate into the phase of projected sinusoidal fringes, so each camera pixel can be matched to a projector pixel. This phase-based correspondence gives FPP sub-pixel accuracy. Despite these advantages, however, FPP still has a critical limitation: focused DLP systems find it difficult to project 8-bit sinusoidal patterns at very high frame rates (Chen et al., 2021; Zheng et al., 2021).

Binary-defocusing FPP addresses this bottleneck by projecting 1-bit patterns in a high-frame-rate binary mode and relying on defocus to recover approximately sinusoidal fringes. The projector defocus acts as a low-pass filter that suppresses high-order harmonics while preserving the fundamental sinusoidal component; this also avoids gamma nonlinearity. To further improve the approximation at moderate defocus, dithering algorithms are used to shape the binary pattern before projection. Among them, error diffusion is a standard choice because it propagates the quantization residual from each processed pixel to neighboring unprocessed pixels, which is especially useful for encoding wide fringes. However, error diffusion was not originally designed for fringe patterns. Its diffusion kernel controls the direction and strength with which the residual error is redistributed, but the relationship between this directional propagation and the final phase error has not been analyzed or optimized. As a result, a poorly chosen kernel can distort the sinusoidal profile and degrade the reconstructed phase.

Reviewers: please read the Reviewer Guidelines (iclr.cc/Conferences/2027/ReviewerGuidelines) and the AI Policy for Reviewers (iclr.cc/Conferences/2027/AIPolicyForReviewers). If you used AI to expand, edit, or polish your review, please provide the input text to the LLM. Better still, consider skipping the LLM and submitting your original text: we, and the authors, are much more interested in your unedited thoughts than in what an LLM has to say. AI-assisted or not, you are putting your name and reputation behind your review: LLM-generated falsehoods, hallucinations or misrepresentations are subject to disciplinary action, which may include desk-rejecting all papers you have authored.

Building on our previous research on defocused systems, we have distilled a set of essential guidelines for designing a reliable error diffusion algorithm. The error diffusion kernel designed according to these guidelines can effectively mitigate the distortion of fringes without requiring additional correction operations, preserving the real-time performance of binary-defocusing FPP. A series of comparison experiments are conducted to validate the accuracy and effectiveness of the proposed algorithm. Our main contributions are summarized as follows:

- We qualitatively analyze the four error-diffusion coefficients separately and show that they contribute differently to the recovered phase error. This per-parameter analysis reveals that the forward and backward components dominate the directional bias.
- We introduce a normalized directional balance coefficient for error-diffusion kernels and show that the first-order phase bias vanishes when the forward and backward propagation strengths are balanced. This is a kernel-level design rule rather than a fringe-specific compensation scheme.
- Based on the above analysis, we propose a set of guidelines that a reliable error diffusion algorithm must satisfy. Comparison experiments demonstrate that these guidelines significantly reduce the phase error caused by error diffusion algorithms. Compared to existing optimization methods, the phase error is reduced by approximately 22.45%.

2 Related Work

Lei & Zhang (2009) observed that optical defocus can act as a low-pass filter and turn a binary pattern into an approximately sinusoidal intensity distribution, an observation that motivates binary-defocusing FPP. To improve the quality of binary fringes, Ayubi et al. (2010) introduced pulse-width modulation (PWM) to suppress high-order harmonics, Wang & Zhang (2010) proposed optimized PWM (OPWM), and Zuo et al. (2012) developed triple-SPWM, which produces near-ideal sinusoidal patterns under weak defocus. After further development, binary fringe encoding methods can be broadly grouped into dithering-based approaches (Ni et al., 2024; Lu et al., 2019) and iterative optimization-based approaches (Zhou et al., 2020; Zhu et al., 2022b).

Among dithering methods, error-diffusion dithering is particularly attractive because it balances the binarization residual across neighboring pixels (Zhu et al., 2022a). This balancing preserves the mean intensity of the pattern and allows wide fringes to be encoded stably even at shallow defocus. Classical algorithms in this family include Floyd-Steinberg (FS) (Floyd & Steinberg, 1976) and Sierra-Lite (Sierra, 1989). Shan et al. (2023) extended and tuned the FS kernel to reduce high-order harmonic distortion. You et al. (2022b) studied the phase error of defocused fringes and proposed fixed phase-offset compensation, while You et al. (2022a) later introduced half-truncated sinusoidal fringes, in which half of the intensity values are set to zero, to simplify binarization. More recently, Chen et al. (2026) proposed an error-diffusion fusion strategy that combines an FS kernel with its inverse for four-step phase-shifting. Iterative methods, by contrast, optimize either the pixel intensities of the fringe pattern (Xiao & Li, 2017; Lu et al., 2019) or the error-diffusion kernel (Xu et al., 2023; Zhu et al., 2024). Pixel-level optimization can achieve high fidelity, but it is usually more time- and memory-consuming than kernel-level optimization. Existing kernel-level methods, however, still do not provide an explicit condition for controlling the directional bias of the kernel.

High-speed FPP has also been advanced from the acquisition and unwrapping sides. Liu & Kofman (2017) encoded background and amplitude into high-frequency fringes, reducing the number of required images. Yin et al. (2019) combined depth constraints with number-theoretical phase unwrapping to retrieve absolute phase at 3333 frames per second. For motion-induced errors, Wang et al. (2018) used a Hilbert transform to generate an additional phase-shifted fringe set and averaged the resulting two phase maps to suppress motion artifacts. Guo et al. (2021) proposed a real-time compensation method for four-step phase-shifting profilometry. These methods improve speed or motion robustness by changing the projection sequence, unwrapping strategy, or post-processing. In contrast, this paper seeks a pre-correction strategy that corrects the directional error at its source, namely the error-diffusion kernel itself, rather than selecting an optimal kernel through iterative optimization. The proposed design is independent of the phase-shifting step and introduces no additional time overhead during reconstruction.

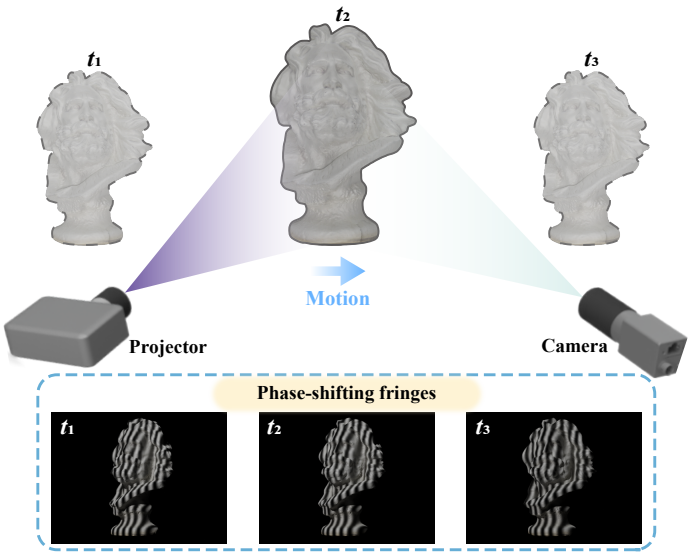

Figure 1: FPP system schematic.

3 KERNEL DIFFUSION MECHANISM

This section first presents the fundamental principles of general diffusion algorithms. It then examines the impact of diffusion kernel parameters on phase errors. Based on Fourier analysis, the explicit form of the phase error is derived, providing a theoretical foundation for establishing an error-diffusion kernel design principle.

3.1 PRELIMINARY KNOWLEDGE

Fig. 1 depicts a standard FPP setup, comprising a camera and a projector. During the measurement process, the DLP projector projects a series of phase-shifting fringe patterns onto the surface of object. These patterns are then captured by the camera, which records the modulation caused by the shape of object. The captured fringe patterns are subsequently decoded and unwrapped to obtain the absolute phase (Zuo et al., 2016). Using the calibration data of the camera and projector, this absolute phase is converted into a 3D point cloud of the measured object. However, object motion during measurement causes positional inconsistencies among the fringes captured at t_1, t_2, and t_3, leading to phase distortion and degraded 3D reconstruction. To improve the projection rate, sinusoidal patterns are binarized via dithering algorithm, which diffuses pixel-wise binarization residual errors to neighboring pixels so that the resulting binary patterns can approximate sinusoidal fringes after projector defocusing. This algorithm can be formulated as follows (You et al., 2022b):

$$\begin{aligned} &I_n(x,y) = a + b\cos[\phi(x,y) + \delta_n] \\ &\hat{I}_n(x,y) = I_n(x,y) + \textstyle\sum_{m=1}^{4} \lambda_m e(x - x_m, y - y_m) / \sum_{m=1}^{4} \lambda_m \\ &B_n(x,y) = H[\hat{I}_n(x,y) - 127.5] \\ &e(x,y) = \hat{I}_n(x,y) - B_n(x,y) \end{aligned} , \tag{1}$$

where, $n = 1, 2, \ldots, N$, and N is the total number of phase-shifting patterns. I_n, $\hat{I}_n$, and B_n denote the n-th sinusoidal pattern, its error-diffused version, and the corresponding binarized pattern, respectively. e denotes the binarization residual error. (x, y) is the pixel coordinate on the projector imaging plane, while (x_m, y_m) specifies the offset from the current pixel to the neighboring pixel from which the residual error is propagated. a and b denote the average intensity and intensity modulation, respectively. ϕ is the unwrapped phase, and $\delta_n = 2\pi(n-1)/N$ is the prescribed phase shift. λ_m denotes the preset error diffusion coefficient in the dithering algorithm, and H is the Heaviside step function. By varying λ_m, different error diffusion algorithms can be formulated.

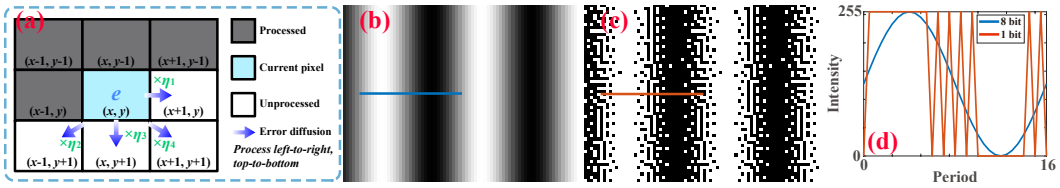

Figure 2: FS dithering algorithm; (a) Schematic of the error diffusion; (b) Original sinusoidal fringe; (c) Binarized fringe after FS dithering algorithm; (d) Line graphs of intensity variation of the fringes before and after binarization.

3.2 Diffusion Coefficient Analysis

In the classical FS dithering algorithm, $(\lambda_1, \lambda_2, \lambda_3, \lambda_4)$ are set to $(7, 3, 5, 1)$. The overall process of FS dithering algorithm is illustrated in Fig. 2(a), where $(\eta_1, \eta_2, \eta_3, \eta_4)$ denote the normalized diffusion coefficients, which can be represented in matrix form as:

$$\Lambda = \begin{pmatrix} - & - & - \\ - & \odot & \eta_1 \\ \eta_2 & \eta_3 & \eta_4 \end{pmatrix} = \frac{1}{\sum_{m=1}^{4} \lambda_m} \begin{pmatrix} - & - & - \\ - & \odot & \lambda_1 \\ \lambda_2 & \lambda_3 & \lambda_4 \end{pmatrix}. \tag{2}$$

$-$ in Eq. (2) is used to indicate previously visited pixels in the binarization, while $\odot$ identifies the current pixel to be binarized. In the actual error diffusion process, these parameters are set to 0. Figs. 2(b) and (c) illustrate the fringe before and after FS binarization, and Fig. 2(d) plots their intensity profiles. It can be seen that FS dithering fails to faithfully reproduce the original fringe in the first half of the period, thereby introducing phase errors. This issue is the primary focus of existing optimization methods and will be addressed in Section 3.3.

$$I_n^g(x, y) = (G * B_n)(x, y). \tag{3}$$

Theoretically, projector defocusing can restore Fig. 2(c) to Fig. 2(b), as shown in Eq. (3). G denotes the projector point spread function characterizing the defocusing process, typically approximated by a two-dimensional Gaussian kernel. However, binarization introduces irreversible information loss, inevitably resulting in phase errors in the restored sinusoidal fringe. Previous studies have indicated that diffusion directions are closely related to phase errors. According to Eq. (2) and Fig. 2(a), the four error diffusion parameters correspond to different diffusion directions. Therefore, the phase error depends not only on the diffusion weights, but also on their directional arrangement. However, existing kernel optimization methods usually treat the diffusion kernel as an integral template for adjustment or iterative optimization, making it difficult to distinguish the contribution of each diffusion direction. This section analyzes the diffusion coefficients from a directional perspective, as shown in Figs. 3(a)-(d). Specifically, the parameters associated with different directions are separated to construct four 1D error diffusion kernels, from which four binarized results of the same original fringe are generated. It is evident that, except for the downward diffusion direction (λ_3), the other diffusion directions do not yield satisfactory binarization results, with some regions failing to form a speckle pattern similar to that in Fig. 2(c). Furthermore, the four binary fringe patterns are restored to sinusoidal fringe patterns using Eq. (3), from which the final phase errors are calculated. The results are summarized in Table 1.

In this table, AE represents the average error, and RMSE denotes the root mean square error. Based on the data in Table 1, the downward diffusion direction associated with λ_3 provides the most stable and reliable error propagation. Notably, this direction is perpendicular to the fringe variation direction, i.e. the phase gradient direction. Accordingly, λ_3 is fixed at a nonzero value in the subsequent experiments to ensure valid error diffusion. Since two-dimensional error diffusion is the core mechanism of dithering, the other three parameters are varied to construct different 2D diffusion kernels, as presented in Fig. 3(e). The phase errors of the resulting binary fringe patterns are calculated to evaluate their performance. In this experiment, four binary fringe patterns with periods of 8, 16, 24, and 32 pixels are generated, and Gaussian filtering with a standard deviation of 3 is used to simulate projector defocusing. Unless otherwise specified, the subsequent simulation experiments follow the same setup.

By observing the variation of AE in the first row of Fig. 3(e), introducing λ_1, λ_2, and λ_4 leads to significant phase errors. Moreover, as their proportions increase, AE gradually decreases from a

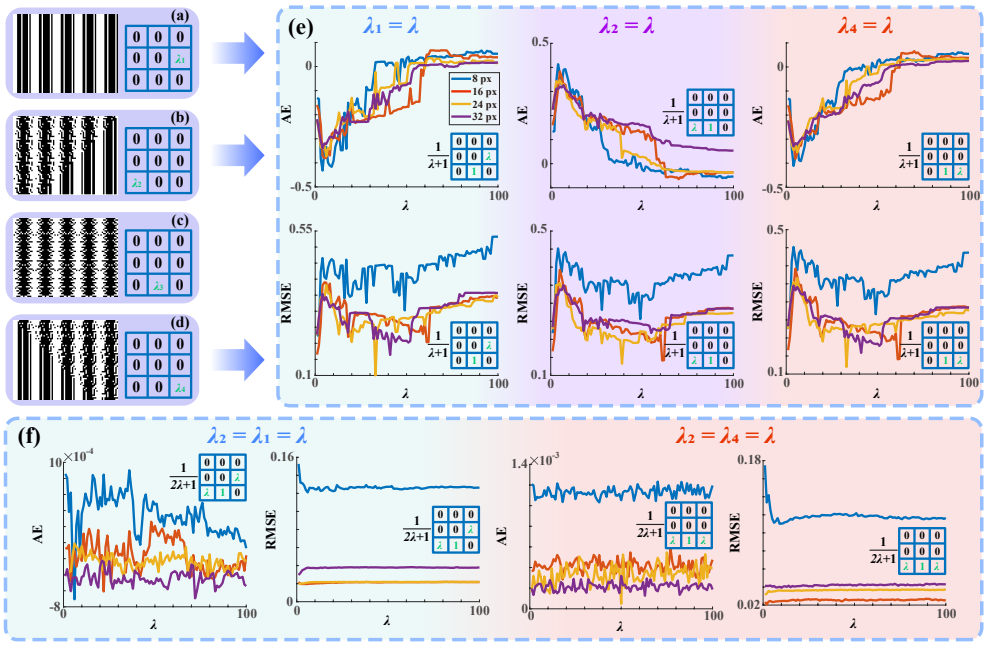

Figure 3: Directional analysis of error diffusion coefficients (Unit: pixel). (a) Rightward diffusion; (b) Lower-left diffusion; (c) Downward diffusion; (d) Lower-right diffusion; (e) Bidirectional error diffusion; (f) Tridirectional error diffusion.

Table 1: Phase errors generated by unidirectional error diffusion (Unit: pixel).

Direction	**Rightward** (λ_1)	**Lower-left** (λ_2)	**Downward** (λ_3)	**Lower-right** (λ_4)
AE	0.0364	-0.0513	0.0001	0.0513
RMSE	0.4099	0.3239	0.0080	0.3206

large value to zero. However, this does not indicate complete error elimination, since the corresponding RMSE curves in the second row of Fig. 3(e) do not decrease significantly. This suggests that directional phase errors are transformed into fluctuating errors. This trend is also reflected in the binary fringes, which gradually transition from Fig. 3(c) to Figs. 3(a), (b), and (d). Therefore, λ_3 should occupy a relatively large proportion in the diffusion kernel. These results also indicate that the directional phase errors introduced by λ_1, λ_2, and λ_4 must be suppressed. As presented in the first row of Fig. 3(e), the errors induced by λ_1 and λ_4 have directions opposite to that induced by λ_2, while their magnitudes are roughly comparable. To examine this characteristic, λ_2 is added to the λ_1 and λ_4 cases in Fig. 3(e), with its value set equal to that of λ_1 or λ_4. The resulting phase-error variations are shown in Fig. 3(f). Compared with Fig. 3(e), both AE and RMSE are significantly reduced, suggesting that λ_2 can effectively counteract the phase errors induced by λ_1 and λ_4. Based on this conclusion, a reliable error-diffusion kernel should satisfy:

$$\eta = (\lambda_1 + \lambda_4 - \lambda_2) / \sum_{m=1}^{4} \lambda_m = 0. \tag{4}$$

where, η denotes the error-diffusion-kernel balance coefficient defined in this paper. Although Eq. (4) is motivated by the preceding directional analysis, it requires broader validation before it can serve as a practical design criterion. Section 3.3 quantifies the relationships among the diffusion parameters, the balance coefficient η, and phase error through extensive simulations and parameter fitting, while Section 4 validates the resulting criterion through physical experiments.

3.3 Parameter Fitting and Design Guidelines

As presented in Fig. 4(a), the binary fringe pattern with a period of 16 pixels generated by the FS dithering algorithm is first restored to a sinusoidal fringe. Since the restored fringe I_n^g still contains

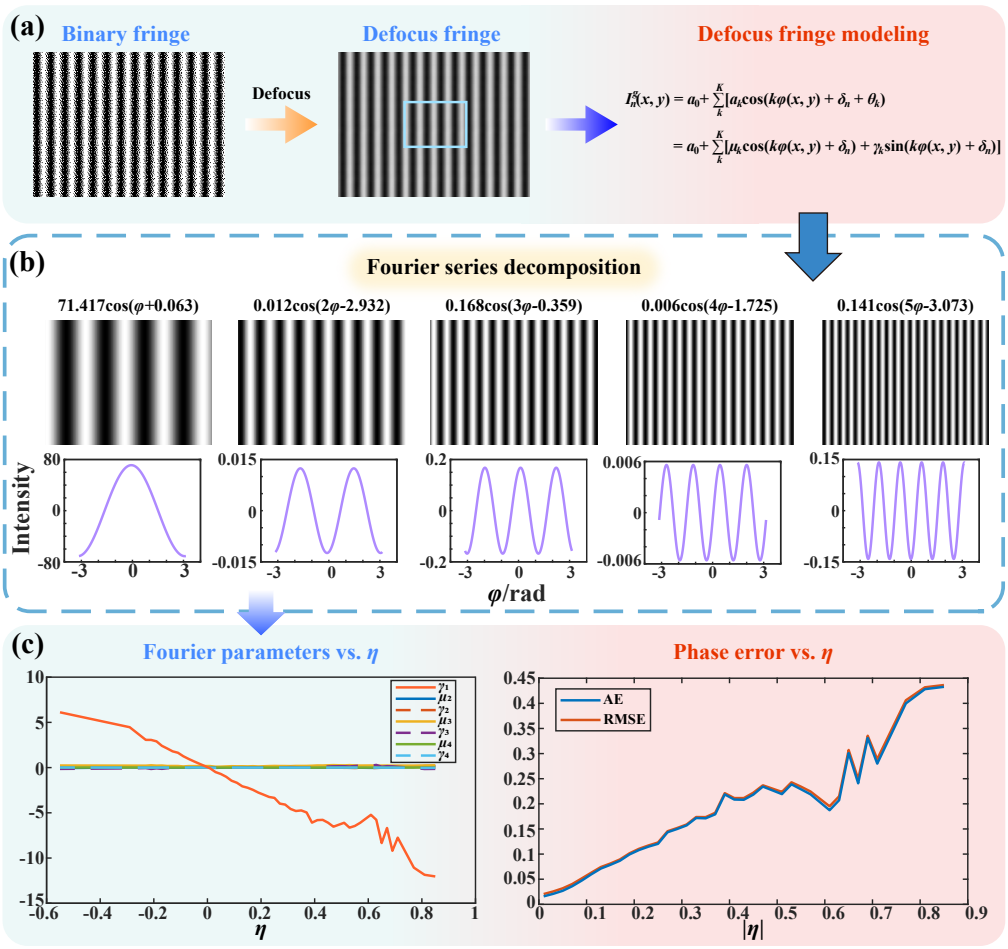

Figure 4: Defocus fringe modeling and analysis: (a) Fourier modeling; (b) Fourier decomposition; (c) Parameter and error analysis.

binarization errors, Fourier expansion is further performed, yielding Eq. (5):

$$I_n^g(x,y) = a_0 + \sum_k^K [\mu_k \cos(k\phi(x,y) + \delta_n) + \gamma_k \sin(k\phi(x,y) + \delta_n)], \tag{5}$$

where, a_0 denotes the DC component of the restored fringe, while μ_k and γ_k denote the coefficients of the cosine and sine terms of the k-th harmonic, respectively. K is the highest harmonic order retained in the Fourier expansion and is typically truncated according to the requirements of the analysis. In this section, a fifth-order Fourier expansion is applied to the restored fringe I_n^g, as presented in Fig. 4(b). The fundamental component obtained after decomposition is given by $71.417\cos(\phi + 0.063)$. The coefficients of its cosine and sine terms are 71.006 and -4.488, respectively. Notably, the cosine term of the fundamental component corresponds to the desired sinusoidal fringe and therefore does not introduce additional error, whereas the coefficient of its sine term (γ_1) remains much larger than those of the higher-order harmonic components. This indicates that the dominant error of the FS algorithm arises from the fundamental sine component in the restored fringe, rather than from higher-order harmonics.

Based on the above procedure, the defocused fringe model under an arbitrary error diffusion kernel can be quantitatively characterized. A total of 298 error diffusion kernels are randomly generated and evaluated. The relationships among the error-diffusion-kernel balance coefficient η, harmonic coefficients μ_k and γ_k, and phase errors are analyzed using a binning strategy, as illustrated in Fig. 4(c). The dominant error term γ_1 is clearly correlated with η, and the phase error follows a similar trend. Eq. (6) presents the RMSE equation fitted with respect to η, based on which the

effects of individual diffusion kernel parameters on the phase error can be further analyzed.

$$\mathrm{RMSE} = -0.021197 + 0.063349\eta_3 + 0.74825|\eta| + 0.11521\eta_3^2 - 0.16518|\eta|^2 - 0.73863|\eta|\eta_3 \quad (6)$$

The fitting uses $|\eta|$ because RMSE and η_3 are non-negative. The two largest-coefficient terms both contain $|\eta|$, and the constant term is small, indicating that $|\eta|$ is the dominant factor affecting the phase error. Differentiating the equation with respect to $|\eta|$ gives:

$$\frac{\partial \mathrm{RMSE}}{\partial |\eta|} = 0.74825 - 0.33036|\eta| - 0.73863\eta_3. \quad (7)$$

Given $|\eta| \in [0, 1]$ and $|\eta| + \eta_3 < 1$, the derivative is always positive, indicating that the error is minimized only at $|\eta| = 0$. When $|\eta| = 0$, the fitted RMSE has a negative constant term, requiring a finite positive η_3 to compensate for it. This gives $\eta_3 \approx 0.23$. This value is not fixed and should be adjusted according to specific configurations. These two observations are consistent with the conclusions summarized in Section 3.2. Moreover, a first-order derivation of why $\eta = 0$ removes the systematic directional phase bias is provided in **Appendix** A.1, and the extension to different periods is reported in **Appendix** A.2.

Based on the results of the analysis and experiments above, the necessary guidelines for designing a reliable error diffusion algorithm can be summarized as follows:

1. Diffusion parameters whose propagation directions are not perpendicular to the fringe variation direction, such as λ_1, λ_2, and λ_4, may introduce directional bias into the restored fringe. Thus, their design should prioritize balancing the total forward and backward diffusion strengths rather than optimizing each parameter independently, i.e., $\lambda_1 + \lambda_4 = \lambda_2$.
2. The parameter λ_3, whose propagation direction is perpendicular to the fringe variation direction, plays an important role in maintaining binarization stability. After λ_1, λ_2, and λ_4 are determined under the balance constraint, λ_3 can be selected through iterative optimization.

4 Experiment

To evaluate the performance of the proposed method in real-world experiments, an FPP measurement system is constructed. The system consists of a computer, a DLP projector, and an industrial camera. The projector is a LightCrafter 4500 from Texas Instruments, and the camera is an acA800-510um from Basler. System calibration is performed using Zhang's calibration method (Zhang, 1999). During the experiments, the wrapped phase was obtained using a four-step phase-shifting method, and phase unwrapping was achieved using complementary Gray-code patterns (Zhang et al., 2012). For comparison, four representative algorithms are evaluated on 16-pixel-period fringes: single optimized kernel diffusion (SOK) (Shan et al., 2023), multi-kernel diffusion (MK) (Xu et al., 2023), half-truncated fringe (HTF) (You et al., 2022a), and fixed phase-bias correction (FPC) (You et al., 2022b). Based on the guidelines summarized in Section 3.3 and the existing optimization algorithm (Zhou et al., 2020), this paper proposes using the error diffusion kernels in Eq. (8) for fringe binarization. Λ_h represents the kernel for horizontal fringes, and Λ_v represents the kernel for vertical fringes. The variation direction of vertical fringes is perpendicular to that of horizontal fringes, resulting in a 90° difference between the kernels. Both kernels ensure that the sum of the parameters for forward propagation is equal to that for backward propagation. For simplicity, this method is referred to as the Guideline Based Optimization (GBO) algorithm in this paper. To ensure the objectivity of the comparison, all experimental conditions remain consistent. Additional experimental results are presented in **Appendix** A.3.

$$\Lambda_h = \frac{1}{42}\begin{pmatrix} - & - & - \\ - & \odot & 11 \\ 12 & 18 & 1 \end{pmatrix}, \Lambda_v = \frac{1}{42}\begin{pmatrix} - & 11 & 1 \\ - & \odot & 18 \\ - & - & 12 \end{pmatrix}, \quad (8)$$

4.1 Experiment on Horizontal Fringe

The first experiment aims to evaluate the performance of the proposed methods in binarizing horizontal fringes. In this experiment, the projector is slightly defocused, and the generated binary

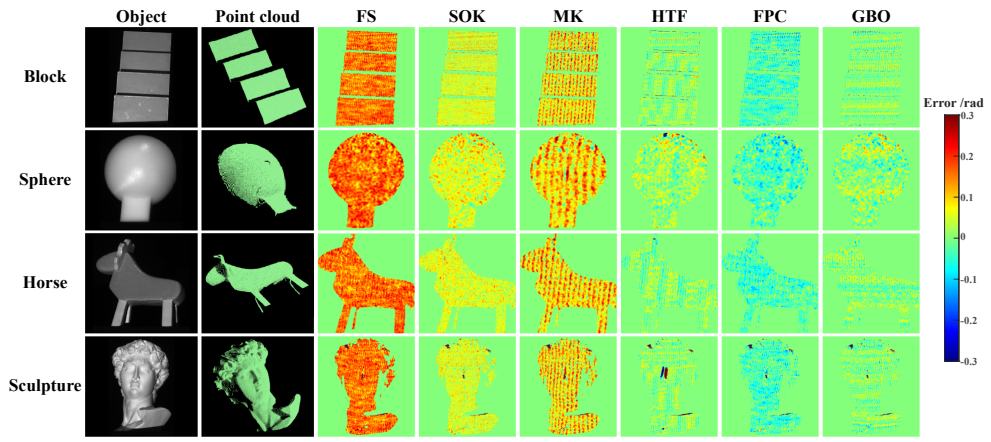

Figure 5: The measured object and reconstructed point cloud, as well as the corresponding horizontal phase error distribution recovered by various methods.

Table 2: AE / RMSE of the recovered horizontal phase (Unit: rad).

Method	FS	SOK	MK	HTF	FPC	GBO
Block	0.155 / 0.160	0.057 / 0.068	0.094 / 0.112	0.037 / 0.087	0.043 / 0.055	**0.030 / 0.041**
Sphere	0.160 / 0.165	0.059 / 0.068	0.098 / 0.112	0.037 / 0.114	0.040 / 0.050	**0.032 / 0.041**
Horse	0.159 / 0.162	0.057 / 0.064	0.098 / 0.113	0.030 / 0.100	0.038 / 0.046	**0.026 / 0.033**
Sculpture	0.164 / 0.183	0.059 / 0.122	0.098 / 0.145	0.334 / 1.789	0.043 / 0.094	**0.032 / 0.077**

fringes are used to measure four different object models: a trapezoidal block, a sphere, a wooden horse model, and the David sculpture. These objects encompass various geometric features, including planes, spheres, and complex curved surfaces. The appearance of the measured objects is presented in the first column of Fig. 5, with the corresponding point clouds in the second column. The horizontal fringes, modulated by the object shapes and captured by the camera, are converted into absolute phase values, and their error distributions are calculated. The error distribution results of different methods are illustrated in the last six columns of Fig. 5. The ground truth of the absolute phase is obtained by projecting the original 8-bit fringes. It can be observed that the FS algorithm indeed introduces directional offset errors. The five optimization methods have achieved varying degrees of improvement, among which HTF, FPC, and GBO demonstrate superior performance. To provide a more comprehensive comparison, the AE and RMSE are calculated, and the detailed data are presented in Table 2. In these tables, boldface indicates the lowest error, while underlining indicates the second-lowest error. HTF achieves better performance in terms of AE but exhibits higher RMSE. As shown in the error distribution of the sculpture in Fig. 5, this is due to significant errors near the object edges, caused by half-truncated fringes. A possible underlying reason is the half-truncation mechanism, which reduces the fringe-carried information by nearly half and consequently weakens the robustness of phase recovery. GBO demonstrates superior stability across varying conditions and achieves the best performance. Compared with the second-best method, AE is reduced by 17.84%, and RMSE is reduced by 22.45% overall.

4.2 Experiment on Vertical Fringe

In principle, vertical fringes in practical experiments can be obtained by transposing horizontal fringes. Thus, ensuring the accurate binarization of horizontal fringes is generally sufficient. However, since the variation direction of vertical fringes differs from that of horizontal fringes, directly binarizing vertical fringes using existing optimization methods can offer deeper insights into the relationship between error diffusion direction and fringe variation direction. This will further validate the accuracy of the guidelines proposed in Section 3.3. Therefore, this experiment evaluates the performance of the aforementioned methods on vertical fringes, with the results presented in Fig. 6. The first column shows the vertical fringes modulated by the object shapes, while the subsequent seven columns display the phase error distributions of various algorithms. Among these, the GBO

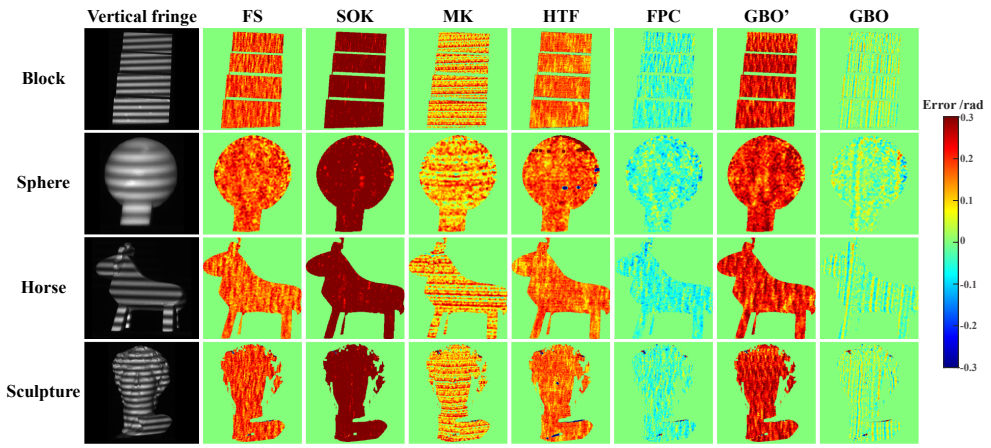

Figure 6: The vertical fringe modulated by the shape of the measured object and the corresponding vertical phase error distribution recovered by various methods.

Table 3: AE / RMSE of the recovered vertical phase (Unit: rad).

Method	FS	SOK	MK	HTF	FPC	GBO
Block	0.185 / 0.191	0.335 / 0.338	0.120 / 0.138	0.166 / 0.188	0.046 / 0.058	**0.041 / 0.053**
Sphere	0.177 / 0.182	0.334 / 0.337	0.116 / 0.128	0.370 / 1.499	0.044 / 0.055	**0.034 / 0.044**
Horse	0.167 / 0.171	0.331 / 0.333	0.116 / 0.133	0.162 / 0.165	0.048 / 0.058	**0.036 / 0.045**
Sculpture	0.191 / 0.196	0.342 / 0.345	0.124 / 0.138	0.180 / 0.401	0.042 / 0.051	**0.036 / 0.046**

uses the error diffusion kernel Λ_v from Eq. (8), while GBO' method employs Λ_h. Detailed error data are provided in Table 3. From the error distributions, it is clear that SOK, MK, HTF, and GBO', which directly apply the error diffusion kernels designed for horizontal fringes to vertical fringes, fail to achieve satisfactory results. In contrast, GBO, utilizing error diffusion kernel specifically designed for vertical fringes, continues to exhibit superior performance. This indicates that the fringe variation direction is closely related to the error of dithering algorithms, further demonstrating the proposed guidelines.

5 Limitations

Several limitations remain in the current study. First, the proposed balance criterion is based on a first-order propagation approximation. Although the first-order term dominates the observed directional phase bias, higher-order terms still remain, especially for small fringe periods or weak projector defocus; extending the criterion to suppress these higher-order terms is an important direction for future work. Second, the projection rate of the projector and the acquisition rate of the camera still bound the achievable measurement speed, so high-speed real-time reconstruction remains constrained by the hardware. Moreover, in dynamic scenes the uncertain motion of the object makes it difficult to obtain reliable ground truth, which limits quantitative comparative experiments in real-world settings.

6 Conclusion

To address directional phase errors in binary-defocusing FPP, this paper introduced a normalized balance coefficient for error-diffusion kernels and derived the condition under which the dominant first-order directional bias vanishes. Based on this criterion, we constructed the Guideline-Based Optimization (GBO) kernels for horizontal and vertical fringes, without changing the phase-shifting fringes or adding reconstruction-time overhead. Experiments on horizontal and vertical fringes show that GBO reduces AE by 17.84% and RMSE by 22.45% relative to the second-best method. The proposed design is independent of the number of phase-shifting steps and does not require iterative kernel optimization, making it a real-time-compatible pre-correction strategy for high-speed FPP.

AI USE STATEMENT

In this work, we used generative AI tools for [assist with translation, edit a research paper to improve readability, format references]. We have not used generative AI tools for [help develop theoretical models or conceptual frameworks, formulate mathematical claims, provide critical ingredients for proving mathematical claims, assist in the writing of proofs, propose or refine hypotheses, design or provide feedback on research methodology or experiments, implement methods, support qualitative and thematic data analysis, interpret results.], and [generate synthetic data sets, clean and reformat dataset] are not applicable to this work. Additionally, we used generative AI tools for [proposing a title and keywords]. We have reviewed all AI-assisted work. [All AI-assisted text modifications and suggestions have been manually checked to ensure their correctness and consistency with the manuscript.] We take responsibility for the final content of this work, including text, claims, or artifacts produced with the aid of generative AI.

ETHICS STATEMENT

[This work does not involve human subjects, animal experiments, personal data, or other foreseeable ethical concerns.]

REPRODUCIBILITY STATEMENT

[We describe the error-diffusion algorithm in Section 3 and the experimental setup in Section 4. The proposed method does not rely on neural networks or complex code design, and all parameter settings are reported in the corresponding sections and tables.]

REFERENCES

Gastón A. Ayubi, Jaime A. Ayubi, J. Matías Di Martino, and José A. Ferrari. Pulse-width modulation in defocused three-dimensional fringe projection. *Optics Letters*, 35(21):3682–3684, 2010.

Xiangcheng Chen, Jun Wu, Ruimei Fan, Qing Liu, Yongxin Xiao, Yuwei Wang, and Yajun Wang. Two-digit phase-coding strategy for fringe projection profilometry. *IEEE Transactions on Instrumentation and Measurement*, 70:1–9, 2021.

Yuchong Chen, Jian Yu, Pengcheng Yao, Shaoyan Gai, and Feipeng Da. Modeling and compensating phase error in high-speed 3d reconstruction. In *Computer Vision – ECCV 2026*. Springer, 2026.

R. W. Floyd and L. Steinberg. An adaptive algorithm for spatial greyscale. *Proceedings of the Society for Information Display*, 17(2):75–77, 1976.

Jason Geng. Structured-light 3d surface imaging: a tutorial. *Adv. Opt. Photon.*, 3(2):128–160, Jun 2011.

Wenbo Guo, Zhoujie Wu, Qican Zhang, and Yajun Wang. Real-time motion-induced error compensation for 4-step phase-shifting profilometry. *Opt. Express*, 29(15):23822–23834, Jul 2021.

Danish Khan, Muhammad Ayaz Shirazi, and Min Young Kim. Single shot laser speckle based 3d acquisition system for medical applications. *Optics and Lasers in Engineering*, 105:43–53, 2018. ISSN 0143-8166.

Junho Koh, Jaekyum Kim, Jin Hyeok Yoo, Yecheol Kim, Dongsuk Kum, and Jun Won Choi. Joint 3d object detection and tracking using spatio-temporal representation of camera image and lidar point clouds. In *Proceedings of the AAAI Conference on Artificial Intelligence*, volume 36, pp. 1210–1218, 2022.

Shuangyan Lei and Song Zhang. Flexible 3-d shape measurement using projector defocusing. *Optics Letters*, 34(20):3080–3082, 2009.

Jintao Li and Xiaojun Cheng. Supervoxel-based extraction and classification of pole-like objects from mls point cloud data. *Optics & Laser Technology*, 146:107562, 2022. ISSN 0030-3992.

Xinran Liu and Jonathan Kofman. Background and amplitude encoded fringe patterns for 3d surface-shape measurement. *Optics and Lasers in Engineering*, 94:63–69, 2017. ISSN 0143-8166.

Feng Lu, Chengdong Wu, and Jikun Yang. Optimized dithering technique for three-dimensional shape measurement with projector defocusing. *Optics Communications*, 430:246–255, 2019. ISSN 0030-4018.

Yubo Ni, Shuai Fu, Chaoyang Su, Zhaozong Meng, Nan Gao, and Zonghua Zhang. Computational grayscale dithering phase measuring deflectomerty for accurate specular surface inspection. *Optics and Lasers in Engineering*, 174:107928, 2024. ISSN 0143-8166.

C. Quan, C.J. Tay, and L.J. Chen. A study on carrier-removal techniques in fringe projection profilometry. *Optics & Laser Technology*, 39(6):1155–1161, 2007. ISSN 0030-3992.

Shuo Shan, Peng Xu, Wen Zhang, Ze Li, Jintao Liu, and Jianhua Wang. Error-diffusion-kernel parameters for binary pattern in 1-bit fringe projection profilometry. *Applied Optics*, 62(33): 8882–8893, 2023.

Frankie Sierra. Sierra and sierra lite error-diffusion dithering algorithms. Usenet post, comp.graphics.algorithms, 1989.

Xianyu Su and Qican Zhang. Dynamic 3-d shape measurement method: A review. *Optics and Lasers in Engineering*, 48(2):191–204, 2010. ISSN 0143-8166. Fringe Projection Techniques.

Y. Wang, Z. Liu, C. Jiang, and S. Zhang. Motion induced phase error reduction using a hilbert transform. *Opt. Express*, 26(26):34224–34235, Dec 2018.

Yajun Wang and Song Zhang. Optimal pulse width modulation for sinusoidal fringe generation with projector defocusing. *Optics Letters*, 35(24):4121–4123, 2010.

Yi Xiao and Youfu Li. High-quality binary fringe generation via joint optimization on intensity and phase. *Optics and Lasers in Engineering*, 97:19–26, 2017. ISSN 0143-8166.

C. Xu, M. Duan, Z. Sun, Y. Zheng, Y. Kan, Y. Jin, and C. Zhu. Flexible error diffusion algorithm for binary defocusing fringe projection profilometry. *IEEE Transactions on Instrumentation and Measurement*, 72:1–12, 2023. ISSN 1557-9662.

Li Yan, Zan Li, Hua Liu, Junxiang Tan, Sainan Zhao, and Changjun Chen. Detection and classification of pole-like road objects from mobile lidar data in motorway environment. *Optics & Laser Technology*, 97:272–283, 2017. ISSN 0030-3992.

Wei Yin, Chao Zuo, Shijie Feng, Tianyang Tao, Yan Hu, Lei Huang, Jiawei Ma, and Qian Chen. High-speed three-dimensional shape measurement using geometry-constraint-based number-theoretical phase unwrapping. *Optics and Lasers in Engineering*, 115:21–31, 2019. ISSN 0143-8166.

Di You, ZhiSheng You, Xiao Zhang, and JiangPing Zhu. High-quality 3d shape measurement with binary half truncated sinusoidal fringe pattern. *Optics and Lasers in Engineering*, 155:107046, 2022a. ISSN 0143-8166.

Di You, ZhiSheng You, Pei Zhou, and JiangPing Zhu. Theoretical analysis and experimental investigation of the floyd-steinberg-based fringe binary method with offset compensation for accurate 3d measurement. *Optics Express*, 30(15):26807–26823, 2022b.

Feihu Zhang, Victor Prisacariu, Ruigang Yang, and Philip H.S. Torr. Ga-net: Guided aggregation net for end-to-end stereo matching. In *2019 IEEE/CVF Conference on Computer Vision and Pattern Recognition (CVPR)*, pp. 185–194, 2019.

Qican Zhang, Xianyu Su, Liqun Xiang, and Xuezhen Sun. 3-d shape measurement based on complementary gray-code light. *Optics and Lasers in Engineering*, 50(4):574–579, 2012. ISSN 0143-8166.

Song Zhang and Shing-Tung Yau. High-resolution, real-time 3d absolute coordinate measurement based on a phase-shifting method. *Opt. Express*, 14(7):2644–2649, Apr 2006.

Zhengyou Zhang. Flexible camera calibration by viewing a plane from unknown orientations. In *Proceedings of the seventh ieee international conference on computer vision*, volume 1, pp. 666–673. Ieee, 1999.

Yabing Zheng, Yi Jin, Minghui Duan, Changan Zhu, and Enhong Chen. Joint coding strategy of the phase domain and intensity domain for absolute phase retrieval. *IEEE Transactions on Instrumentation and Measurement*, 70:1–8, 2021.

Peng Zhou, Ning Cai, Ting Wang, Xiang-Qun Cao, and Bin Lin. High-quality 3d shape measurement by kernel-optimized high sinusoidal similarity dither patterns. *Applied Optics*, 59(34): 10645–10650, 2020.

J. Zhu, C. Zhu, P. Zhou, Z. He, and D. You. An optimizing diffusion kernel-based binary encoding strategy with genetic algorithm for fringe projection profilometry. *IEEE Transactions on Instrumentation and Measurement*, 71:1–8, 2022a. ISSN 1557-9662.

J. Zhu, J. Luo, J. Du, and P. Zhou. Spatial–temporal binarization method via jointly optimizing diffusion kernel and quantization threshold for 3-d surface imaging. *IEEE Transactions on Instrumentation and Measurement*, 73:1–13, 2024. ISSN 1557-9662.

Sijie Zhu, Yiping Cao, Qican Zhang, and Yajun Wang. High-efficiency and robust binary fringe optimization for superfast 3d shape measurement. *Optics Express*, 30(20):35539–35553, 2022b.

Chao Zuo, Qian Chen, Shijie Feng, Fangxiaoyu Feng, Guohua Gu, and Xiubao Sui. Optimized pulse width modulation pattern strategy for three-dimensional profilometry with projector defocusing. *Applied Optics*, 51(19):4477–4490, 2012.

Chao Zuo, Lei Huang, Minliang Zhang, Qian Chen, and Anand Asundi. Temporal phase unwrapping algorithms for fringe projection profilometry: A comparative review. *Optics and Lasers in Engineering*, 85:84–103, 2016. ISSN 0143-8166.

A Appendix

A.1 Derivation of the Balance Condition

This appendix presents the first-order derivation underlying the balance condition introduced in Section 3.2. The objective is to clarify why $\eta = 0$ eliminates the systematic directional phase bias caused by error diffusion.

For the n-th sinusoidal fringe, the error-diffusion process can be formulated as

$$\begin{cases} \hat{I}_n = I_n + \mathcal{D}e, \\ B_n = H[\hat{I}_n - 127.5], \\ e = \hat{I}_n - B_n, \end{cases} \tag{9}$$

where, $\mathcal{D}$ denotes the normalized diffusion operator:

$$(\mathcal{D}e)(x,y) = \sum_{m=1}^{4} \eta_m e(x - x_m, y - y_m), \qquad \eta_m = \frac{\lambda_m}{\sum_{j=1}^{4} \lambda_j}. \tag{10}$$

By substituting $e = \hat{I}_n - B_n$ into $\hat{I}_n = I_n + \mathcal{D}e$, the binary fringe can be rewritten as

$$B_n = I_n + (\mathcal{D} - \mathcal{I})e, \tag{11}$$

where, $\mathcal{I}$ is the identity operator. Since projector defocus G acts as a low-pass filter, the phase error is mainly determined by the low-frequency component of the residual error. For a slowly varying residual, its first-order Taylor expansion is

$$e(x - x_m, y - y_m) \approx e(x,y) - x_m \frac{\partial e}{\partial x} - y_m \frac{\partial e}{\partial y}. \tag{12}$$

By using $\sum_m \eta_m = 1$, the diffusion operation can be approximated as

$$\mathcal{D}e \approx e - \mathbf{M} \cdot \nabla e, \tag{13}$$

where, the first-order moment vector of the diffusion kernel is defined as

$$\mathbf{M} = \sum_{m=1}^{4} \eta_m (x_m, y_m) = \left(\sum_{m=1}^{4} \eta_m x_m, \sum_{m=1}^{4} \eta_m y_m \right). \tag{14}$$

Consequently, the first-order approximation of the residual term becomes

$$(\mathcal{D} - \mathcal{I})e \approx -\mathbf{M} \cdot \nabla e. \tag{15}$$

After defocusing, the intensity error introduced by binarization is approximately

$$\Delta I_n = G * B_n - G * I_n \approx -G * (\mathbf{M} \cdot \nabla e). \tag{16}$$

For an N-step phase-shifting algorithm, the first-order phase error is

$$\Delta\phi \propto \sum_{n=0}^{N-1} \sin(\phi + \delta_n) \Delta I_n \approx -\sum_{n=0}^{N-1} \sin(\phi + \delta_n) G * (\mathbf{M} \cdot \nabla e). \tag{17}$$

For horizontal fringes, the phase variation occurs along the x direction; therefore, the first-order moment along the x direction mainly determines the systematic phase bias.

$$\Delta\phi^{(x)} \propto -M_x \sum_{n=0}^{N-1} \sin(\phi + \delta_n) G * \frac{\partial e}{\partial x}. \tag{18}$$

For horizontal fringes, the systematic bias is therefore controlled by

$$M_x = \sum_{m=1}^{4} \eta_m x_m. \tag{19}$$

For the kernel layout adopted in this paper,

$$\lambda_1 : (+1, 0), \quad \lambda_2 : (-1, +1), \quad \lambda_3 : (0, +1), \quad \lambda_4 : (+1, +1), \tag{20}$$

the horizontal first-order moment becomes

$$M_x = \eta_1 - \eta_2 + \eta_4 = \frac{\lambda_1 + \lambda_4 - \lambda_2}{\sum_{j=1}^{4} \lambda_j} = \eta. \tag{21}$$

Thus,

$$M_x = 0 \quad \Longleftrightarrow \quad \lambda_1 + \lambda_4 = \lambda_2 \,. \tag{22}$$

This condition reveals the physical meaning of the proposed balance criterion: the first-order moment of the diffusion kernel along the phase-gradient direction is forced to zero, thereby eliminating the systematic directional phase bias introduced by binarization. The parameter λ_3 only contributes to the moment perpendicular to the phase-gradient direction and therefore does not affect M_x. Instead, it influences the stability of the binarization process and higher-order residual characteristics, and can be optimized independently after satisfying the balance constraint.

A.2 Multi-period and Multi-defocus Analysis

To further evaluate the generality of the proposed design criterion under diverse operating conditions, we extend the single-period analysis to a multi-period and multi-defocus simulation study. The fringe period is varied from 5 to 150 pixels with an interval of 1 pixel. The projector defocus is modeled using a two-dimensional Gaussian point spread function, where the standard deviation σ ranges from 0.5 to 10 pixels with a step size of 0.1 pixels. The compared methods are GBO, FS, FPC, SOK, HTF, and MK. The original 8-bit grayscale sinusoidal fringes are used as the reference for phase error evaluation. The simulated fringe patterns have a resolution of 256×384 pixels, and the RMSE is calculated for each configuration.

Since the absolute error magnitudes vary considerably across different conditions, the RMSE values are first transformed to logarithmic scale and then normalized for visualization:

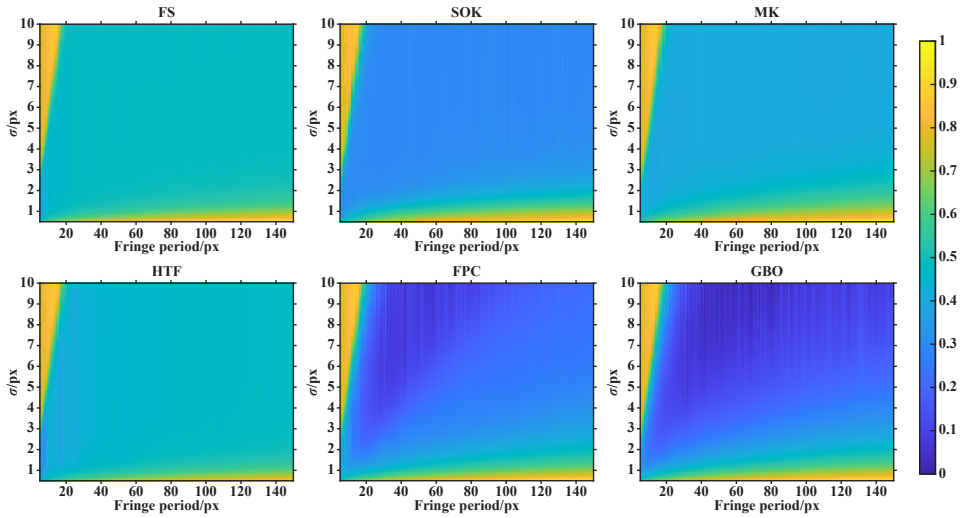

Figure 7: Normalized RMSE distributions of different methods under varying fringe periods and projector defocus levels.

$$\hat{\mathrm{RMSE}} = \mathrm{Norm}(\log_{10}\mathrm{RMSE}) = \frac{\log_{10}\mathrm{RMSE} - \log_{10}\mathrm{RMSE}_{\min}}{\log_{10}\mathrm{RMSE}_{\max} - \log_{10}\mathrm{RMSE}_{\min}}, \tag{23}$$

where, $\mathrm{RMSE}_{\min}$ and $\mathrm{RMSE}_{\max}$ denote the global minimum and maximum RMSE values among all evaluated methods. After normalization, all error values are mapped into the range $[0, 1]$, allowing different subplots to share an identical color scale. Fig. 7 presents the normalized RMSE distributions, with the fringe period as the horizontal axis and the defocus parameter σ as the vertical axis.

As presented in Fig. 7, all methods exhibit two high-error regions located near the upper-left and lower-right corners. The upper-left region corresponds to strong defocusing, where the defocus range exceeds one fringe period and causes gray-level aliasing between adjacent periods. In contrast, the lower-right region appears under large fringe periods, where the relatively weak defocusing effect cannot sufficiently suppress the residual binarization error. Excluding these extreme cases, GBO consistently maintains lower phase errors over a broad range of fringe periods and defocus levels, demonstrating the robustness of the proposed balance coefficient and its associated kernel design criterion.

A.3 Additional Experiments

All experiments in this work are conducted using the same FPP system, whose configuration is shown in Fig. 8. The system consists of a digital projector and a camera. The projector projects encoded fringe patterns onto the object surface, and the camera captures the deformed fringe patterns for phase reconstruction.

Point cloud reconstruction. To examine whether the phase-level improvement of GBO is preserved in the final 3D geometry, we reconstruct the point clouds of three representative objects, namely cross, dog, and bust, under the same experimental configuration as Section 4. All settings remain identical across methods. Fig. 9 presents the measured objects, their reconstructed point clouds, and the corresponding error distributions, while Table 4 summarizes the MAE and RMSE for all methods. GBO consistently yields the lowest errors for all three objects. HTF achieves competitive MAE values on several objects, but its RMSE increases sharply on Dog and Bust, indicating that half-truncated fringes introduce stronger localized outliers. In contrast, GBO maintains low MAE and RMSE simultaneously, confirming that the proposed balance criterion effectively suppresses directional phase bias. Averaged over the three objects, GBO reduces MAE and RMSE by 23.69% and 18.50%, respectively, compared with FPC, which exhibits relatively consistent reconstruction performance among the compared methods.

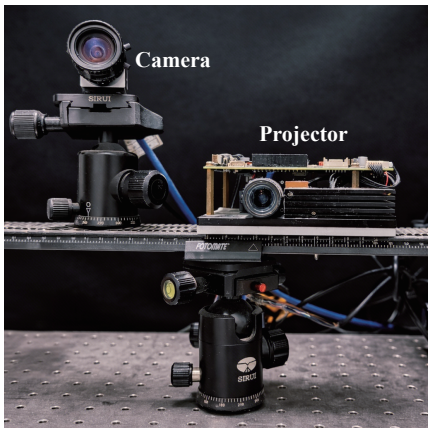

Figure 8: Configuration of the FPP system.

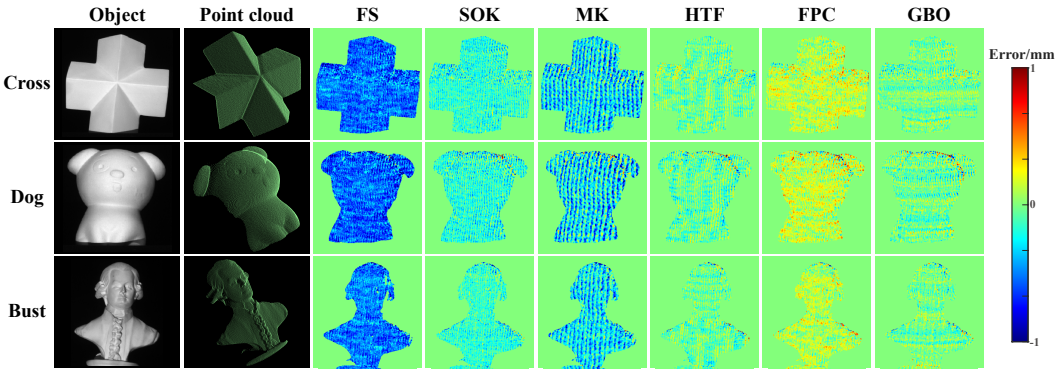

Figure 9: Point cloud reconstruction results and error distributions of Cross, Dog, and Bust.

Table 4: MAE / RMSE of the reconstructed point clouds (Unit: mm).

Method	FS	SOK	MK	HTF	FPC	GBO
Cross	0.265 / 0.391	0.089 / 0.150	0.154 / 0.262	0.055 / 0.099	0.070 / 0.123	**0.050 / 0.092**
Dog	0.286 / 0.539	0.102 / 0.334	0.159 / 0.398	0.076 / 1.014	0.080 / 0.367	**0.062 / 0.313**
Bust	0.214 / 0.344	0.073 / 0.237	0.125 / 0.229	0.061 / 1.188	0.055 / 0.109	**0.044 / 0.092**

Three-Step Phase Shifting. To examine whether the proposed design criterion depends on the number of phase-shifting steps, we perform three-step phase-shifting measurements on two objects, figurine and vase. Except that the fringe period is adjusted to 15 pixels, all other experimental settings remain identical to those in the four-step experiments. Fig. 10 presents the measured objects and their reconstruction error distributions, while Table 5 reports the MAE and RMSE results of the compared methods. HTF is excluded from this table since it requires four-step phase-shifting patterns. GBO achieves the lowest errors for both objects. Specifically, GBO reduces the MAE/RMSE by 17.54%/16.00% for Figurine compared with FPC, and achieves MAE and RMSE reductions of 25.00% and 21.74% for Vase compared with FPC and SOK, respectively.

These results are particularly important because many classical correction methods are developed for four-step or higher-order phase-shifting schemes and cannot be directly applied to the fastest three-step measurement. In contrast, GBO optimizes the error-diffusion kernel during the fringe encoding stage and is independent of the number of phase-shifting steps. Therefore, the proposed method effectively suppresses binary quantization errors for phase-shifting measurements with different numbers of phase-shifting steps, without requiring any additional computation or post-processing during measurement, making it highly suitable for high-speed 3D measurement.

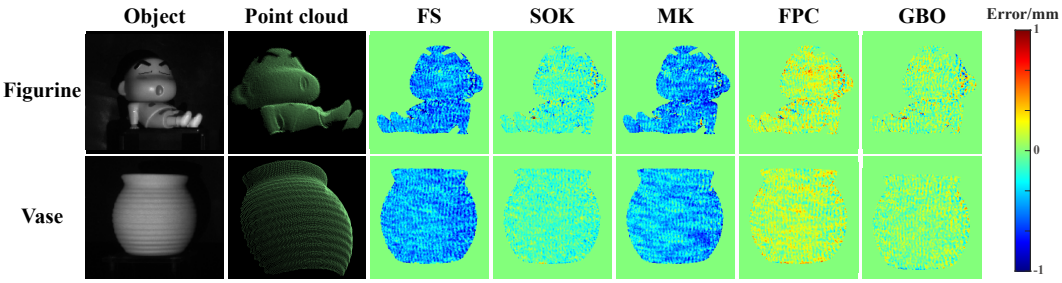

Figure 10: Three-step phase-shifting measurements of Figurine and Vase.

Table 5: MAE / RMSE of the reconstructed objects under three-step phase shifting (Unit: mm).

Object	FS	SOK	MK	FPC	GBO
Figurine	0.175 / 0.304	0.059 / 0.125	0.168 / 0.295	0.057 / 0.125	**0.047 / 0.105**
Vase	0.253 / 0.342	0.073 / 0.115	0.223 / 0.307	0.072 / 0.116	**0.054 / 0.090**

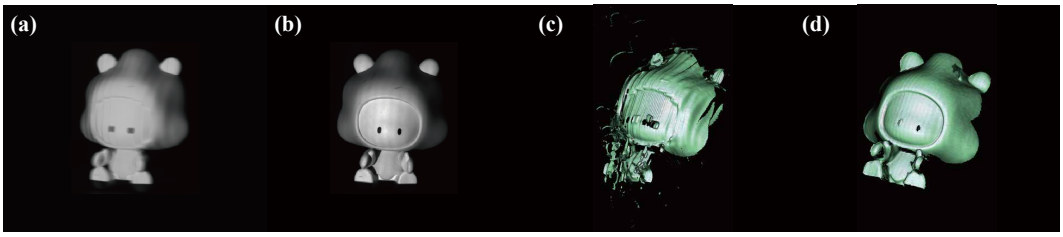

Figure 11: Dynamic measurement results using conventional sinusoidal projection and the proposed GBO binary fringe projection. (a) Averaged intensity of 8-bit sinusoidal patterns; (b) Averaged intensity of GBO; (c) reconstructed point cloud using 8-bit sinusoidal projection; (d) reconstructed point cloud using GBO.

Dynamic Measurement. To further verify the practical robustness of GBO under high-speed measurement conditions, a dynamic experiment is conducted using conventional sinusoidal projection and GBO-based binary fringe projection. During motion, the object position changes within the acquisition period, causing spatial inconsistency among the captured phase-shifting patterns. Fig. 11 compares the measurement results obtained using the two projection strategies. For conventional sinusoidal projection, its averaged intensity in Fig. 11(a) exhibits obvious motion-induced blur. The corresponding reconstructed point cloud in Fig. 11(c) contains severe outliers and geometric distortions, mainly caused by phase recovery errors due to inter-frame motion. In contrast, the GBO binary fringe projection in Fig. 11(b) maintains clearer fringe information during motion, and the reconstructed point cloud in Fig. 11(d) preserves the overall 3D shape with substantially fewer artifacts. Since all binary-defocusing methods share the same high-speed acquisition advantage, this experiment is not intended to compare different binary encoding strategies. Instead, it verifies that GBO can preserve accurate phase reconstruction under dynamic measurement conditions.